

## RESEARCH ARTICLE

# The MAGPI Survey: Insights into the Ly $\alpha$ line widths and the size of ionized bubbles at the edge of cosmic reionization

T. Mukherjee<sup>1,2,3</sup> T. Zafar<sup>1,2,3</sup> T. Nanayakkara<sup>4,2</sup> A. Gupta<sup>5,2</sup> S. Gurung-Lopez<sup>6,7</sup> A. Battisti<sup>8,2</sup> E. Wisnioski<sup>8,2</sup> C. Foster<sup>9,2</sup> J. T. Mendel<sup>8,2</sup> K. E. Harborne<sup>10,2</sup> C. D. P. Lagos<sup>10,2</sup> T. Kodama<sup>11</sup> S. M. Croom<sup>12,2</sup> S. Thater<sup>13</sup> J. Webb<sup>1,3</sup> S. Barsanti<sup>14,2,15</sup> S. M. Sweet<sup>16,2</sup> J. Prathap<sup>1,2,3</sup> L. M. Valenzuela<sup>17</sup> A. Mailvaganam<sup>1,2,3</sup> and J. L. Carrillo Martinez<sup>1,2,3</sup>

<sup>1</sup>School of Mathematical and Physical Sciences, Macquarie University, NSW 2109, Australia

<sup>2</sup>ARC Centre of Excellence for All Sky Astrophysics in 3 Dimensions (ASTRO 3D)

<sup>3</sup>Astrophysics and Space Technologies Research Centre, Macquarie University, Sydney, NSW 2109, Australia

<sup>4</sup>Centre for Astrophysics and Supercomputing, Swinburne University of Technology, PO Box 218, Hawthorn 3122, VIC, Australia

<sup>5</sup>International Centre for Radio Astronomy Research (ICRAR), Curtin University, Bentley, WA, Australia

<sup>6</sup>Observatori Astronòmic de la Universitat de València, Ed. Instituts d'Investigació, Parc Científic. C/ Catedrático José Beltrán, n2, 46980 Paterna, Valencia, Spain

<sup>7</sup>Departament d'Astronomia i Astrofísica, Universitat de València, 46100 Burjassot, Spain

<sup>8</sup>Research School of Astronomy and Astrophysics, Australian National University, Canberra, ACT 2611, Australia

<sup>9</sup>School of Physics, University of New South Wales, Sydney, NSW 2052, Australia

<sup>10</sup>International Centre for Radio Astronomy Research (ICRAR), The University of Western Australia, Crawley, WA 6009, Australia

<sup>11</sup>Astronomical Institute, Tohoku University, 6-3 Aramaki, Aoba-ku, Sendai 980-8578, Japan

<sup>12</sup>Sydney Institute for Astronomy, School of Physics, University of Sydney, NSW 2006, Australia

<sup>13</sup>Department of Astrophysics, University of Vienna, Türkenschanzstraße 17, 1180 Vienna

<sup>14</sup>Research School of Astronomy and Astrophysics, Australian National University, Canberra, ACT 2611, Australia

<sup>15</sup>Sydney Institute for Astronomy, School of Physics, University of Sydney, NSW 2006, Australia

<sup>16</sup>School of Mathematics and Physics, University of Queensland, Brisbane, QLD 4072, Australia

<sup>17</sup>Universitäts-Sternwarte, Fakultät für Physik, Ludwig-Maximilians-Universität München, Scheinerstr. 1, 81679 München, Germany

**Author for correspondence:** T. Mukherjee, Email: tamal.mukherjee@hdr.mq.edu.au.

## Abstract

We present spectroscopic properties of 22 Ly $\alpha$  emitters (LAEs) at  $z = 5.5 - 6.6$  with Ly $\alpha$  luminosity  $\log(L_{\text{Ly}\alpha} [\text{erg s}^{-1}]) = 42.4 - 43.5$ , obtained using VLT/MUSE as part of the Middle Ages Galaxy Properties with Integral Field Spectroscopy (MAGPI) survey. Additionally, we incorporate broad-band photometric data from the Subaru Hyper Suprime-Cam (HSC) Wide layer for 17 LAEs in our sample. The HSC- $\gamma$  band magnitudes show that our LAEs are UV-bright, with rest-frame absolute UV magnitudes  $-19.74 \leq M_{\text{UV}} \leq -23.27$ . We find that the Ly $\alpha$  line width increases with Ly $\alpha$  luminosity, and this trend becomes more prominent at  $z > 6$  where Ly $\alpha$  lines become significantly broadened ( $\gtrsim 260 \text{ km s}^{-1}$ ) at luminosities  $\log(L_{\text{Ly}\alpha} [\text{erg s}^{-1}]) > 43$ . This broadening is consistent with previous studies, suggesting that these sources are located inside larger ionized bubbles. We observe a slightly elevated ionizing photon production efficiency estimated for LAEs at  $z > 6$ , which indicates that younger galaxies could be producing more ionizing photons per UV luminosity. A tentative anti-correlation between ionizing photon production efficiency and Ly $\alpha$  rest-frame equivalent width is noticed, which could indicate a time delay between production and escape of ionizing photon primarily due to supernovae activity. Furthermore, we find a positive correlation between radius of ionized regions and Ly $\alpha$  line width, which again suggests that large ionized bubbles are created around these LAEs, which are allowing them to self-shield from the scattering effects of the intergalactic medium. We also detect two very closely separated LAEs at  $z = 6.046$  (projected spatial distance between the cores is 15.92 kpc). This is the LAE pair with the smallest separation ever discovered in the reionization epoch. The size of their respective bubbles suggests that they likely sit inside a common large ionized region. Such a closely-separated LAE pair increases the size of ionized bubble, potentially allowing a boosted transmission of Ly $\alpha$  through neutral intergalactic medium and also supports an accelerated reionization scenario.

**Keywords:** cosmology: dark ages, reionization, first stars – galaxies: evolution, high redshift, intergalactic medium

## 1. Introduction

Cosmic reionization, a pivotal epoch in the history of the Universe, marks the last phase transition of the Universe when neutral hydrogen (H I) in the intergalactic medium (IGM) became fully ionized, ending the cosmic “Dark Ages.” However, the precise timing of reionization and sources capable of emitting sufficient ionizing photons remain subjects of active debate till date. Previously, it was believed that reionization

was largely complete by  $z \sim 6$  (Fan et al., 2006). However, recent studies suggest a relatively late end of reionization at  $z \sim 5.3 - 5.5$  (Becker et al., 2015; Kulkarni et al., 2019; Cain et al., 2021; Bosman et al., 2022). A common belief is that galaxies which are faint in intrinsic ultraviolet (UV) radiation are the primary contributors of reionization, typically releasing about 10 % of their Lyman continuum (LyC) photons (see Finkelstein et al., 2019; Dayal et al., 2020). However, to ex-

plain the relatively rapid decrease in the neutral IGM fraction in later epochs, it is possible that more infrequent luminous sources might also have played a significant role (see [Naidu et al., 2020](#)).

Due to the attenuation of UV photons below the Lyman break by the increasingly neutral IGM at  $z > 4$  (e.g. [Inoue et al., 2014](#); [Steidel et al., 2018](#)), direct observation of LyC photons is almost impossible. Reionization models suggest that a minimum escape fraction of LyC photons,  $f_{\text{esc}}^{\text{LyC}} \gtrsim 10\%$  is required to complete reionization ([Robertson et al., 2015](#); [Finkelstein et al., 2019](#)). Therefore, it is crucial to comprehend how LyC photons escape into the IGM and subsequently ionize it during the epoch of reionization (EoR). Several studies have attempted to make connection between  $f_{\text{esc}}^{\text{LyC}}$  and nebular emission line features such as [O III], C IV, C III] Mg II etc (see, [Izotov et al., 2020](#); [Nakajima et al., 2020](#); [Schaerer et al., 2022](#); [Katz et al., 2022](#); [Xu et al., 2022](#); [Mascia et al., 2023](#); [Choustikov et al., 2024](#)).

The Ly $\alpha$  emission line of atomic hydrogen has been identified as the most reliable indirect tracer of LyC leakage and is used as one of the promising probes of the EoR ([Kakiichi et al., 2016](#); [Laursen et al., 2019](#); [Tang et al., 2023](#)). A rapid decline in the fraction of Ly $\alpha$  emitting galaxies (LAEs) towards higher redshifts ( $z > 5$ ) has been interpreted as a rapid escalation in the H I fraction with increasing redshift ([Pentericci et al., 2011](#); [Tilvi et al., 2014](#); [Stark et al., 2017](#); [Hoag et al., 2019](#); [Whitler et al., 2020](#); [Jones et al., 2024](#); [Nakane et al., 2024](#); [Napolitano et al., 2024](#); [Tang et al., 2024a](#)). Both the observed intensity and shape of the Ly $\alpha$  line offer delicate insights into the proportion of H I within the IGM ([Robertson et al., 2010](#)). The Ly $\alpha$  rest-frame equivalent width ( $\text{EW}_0$ ) has been identified as an excellent indicator of Ly $\alpha$  escape fraction ( $f_{\text{esc}}^{\text{Ly}\alpha}$ ; see [Matthee et al. 2017b](#); [Begley et al. 2024](#); [Tang et al. 2024b](#)). The separation between the blue and red peaks in the double-peak emission can be used to infer H I column densities ( $N_{\text{HI}}$ ), consequently, the escape of LyC photons (see, [Verhamme et al., 2015, 2017](#); [Izotov et al., 2018](#); [Naidu et al., 2022](#)). Furthermore, the detection of a stronger blue-peak profile also indicates a very low column density channel of H I that can leak LyC photons (see, [Furtak et al., 2022](#); [Mukherjee et al., 2023](#)). However, the blue-peak is expected to be scattered away by the neutral IGM at  $z > 5$  ([Hu et al., 2010](#); [Hayes et al., 2021](#)), leaving only a single-peak red-skewed profile.

Narrow-band (NB) surveys have discovered a substantial sample of LAE at  $z = 5.7$  and  $z = 6.6$  (see [Hu et al., 2010](#); [Matthee et al., 2015](#); [Santos et al., 2016](#); [Bagley et al., 2017](#); [Konno et al., 2018](#); [Taylor et al., 2020, 2021](#)), and several LAE have also been detected at  $z = 6.9$  ([Hu et al., 2017](#)) and  $z = 7.3$  ([Konno et al., 2014](#)). Recent data from the James Webb Space Telescope (JWST) has also contributed to the unprecedented characterization of LAEs throughout the EoR ([Tang et al., 2023](#); [Jung et al., 2024](#); [Witten et al., 2024](#)). The advent of giant imagers, such as Subaru/ Hyper Suprime-Cam (HSC; [Miyazaki et al., 2018](#)), has allowed detections of several rare ultra-luminous LAEs (ULLAEs) with  $\log(L_{\text{Ly}\alpha} [\text{erg s}^{-1}]) > 43.5$  (see, [Songaila et al., 2022](#)), including the detections of

extremely rare double-peaked LAEs with a blue-wing (see [Hu et al., 2016](#); [Songaila et al., 2018](#); [Meyer et al., 2021](#)).

The Multi Unit Spectroscopic Explorer (see, [Bacon et al., 2010](#)) on the Very Large Telescope (VLT) has been instrumental in identifying faint LAEs during the EoR (up to  $z \sim 6.6$ ) by providing deep, high-resolution spectral data across a wide field of view, without any redshift restrictions of NB imaging (see, [Hashimoto et al., 2017](#); [Urrutia et al., 2019](#); [Kerutt et al., 2022](#); [Bacon et al., 2023](#)).

Reionization is known to be an inhomogeneous process ([Pentericci et al., 2014](#); [Becker et al., 2015](#); [Bosman et al., 2022](#)), indicating that galaxies in denser regions are likely to create the first 'ionized bubbles' in the Universe ([Mason et al., 2018](#); [Endsley et al., 2021a](#); [Jung et al., 2022b](#); [Endsley & Stark, 2022](#); [Whitler et al., 2024](#)), which then preferentially emit Ly $\alpha$  radiation once they reach a significant size. As a result, the most distant LAEs are vital for observing and mapping the reionization process. Strong Ly $\alpha$  emission at  $z \gtrsim 6$  often indicates the presence of large ionized bubbles in an otherwise neutral IGM, providing direct observational insights into the reionized regions of the early Universe. When Ly $\alpha$  photons are emitted from galaxies located within large ionized bubbles, they undergo cosmological redshifting far into the damping wing before encountering neutral hydrogen. As a result, they transmit more effectively through IGM ([Weinberger et al., 2018](#); [Mason & Gronke, 2020](#); [Smith et al., 2022](#); [Qin et al., 2022](#)). Recent studies have found that Ly $\alpha$  line width increases with luminosity and this trend becomes more prominent at  $z = 6.6$  (see, [Matthee et al., 2017b](#); [Songaila et al., 2024](#)), where higher-luminosity LAEs with  $\log(L_{\text{Ly}\alpha} [\text{erg s}^{-1}]) \gtrsim 43.25$  show significantly broad Ly $\alpha$  lines ([Songaila et al., 2024](#)). At higher redshifts, the IGM becomes more neutral, increasing Ly $\alpha$  line scattering and hence narrowing of the lines is expected. The lack of this effect in brighter LAEs suggests that they reside in more ionized regions, shielding themselves from scattering.

One of the key components in determining the ionizing photon budget is the ionizing photon production efficiency ( $\xi_{\text{ion}}$ ), which is defined as the ratio between the production rate of ionizing photons over the non-ionizing UV luminosity density. It has been found that as we delve deeper into the universe's history, young galaxies seem to appear more efficient in producing ionizing photons (see, [Bouwens et al., 2016](#); [Endsley et al., 2021b](#); [Prieto-Lyon et al., 2023](#); [Simmonds et al., 2023](#); [Tang et al., 2023](#)). Moreover, UV-faint galaxies with Ly $\alpha$  emission are found to have enhanced  $\xi_{\text{ion}}$  ([Masada et al., 2020](#); [Ning et al., 2023](#); [Saxena et al., 2024](#); [Lin et al., 2024](#)) at  $z \sim 6$ , making LAEs in the reionization era the most exciting sources for studying and constraining reionization.

In this paper, we present spectroscopic properties of 22 new LAEs at the end of reionization ( $z = 5.5 - 6.6$ ) found in the MUSE data obtained as a part of the Middle Ages Galaxy Properties with Integral Field Spectroscopy (MAGPI) survey ([Foster et al., 2021](#)). We restrict this current study to redshifts of  $z \gtrsim 5.5$ , considering the global neutral hydrogen fraction approaches  $x_{\text{HI}} \sim 0$  at around  $z \sim 5.5$  in 'late' reionization sce-

narios (Kulkarni et al., 2019; Bosman et al., 2022). We constrain the evolution of Ly $\alpha$  line width as a function of Ly $\alpha$  luminosity up to  $z \sim 7$ . Using spectroscopic information of these LAEs, along with the Subaru Hyper-Suprime Cam (HSC) optical photometric information, we estimate their ionising photon contribution toward the global reionization budget. We also estimate the size of ionized bubbles around these LAEs to investigate the mechanism leading to the visibility of strong Ly $\alpha$  emission even beyond  $z > 6$ .

The layout of this paper is as follows: In §2, we describe the reduction and selection of MUSE data of potential LAE candidates along with the extraction of HSC photometric magnitudes. §3 explores the data analyses: Ly $\alpha$  line fitting and spectroscopic and photometric measurements. §4 presents results on the evolution of the Ly $\alpha$  line widths and give an insight into the potential ionized bubbles surrounding these LAEs and also discusses these findings in context of previous works. The main conclusions and summary of this study are presented in §5. Throughout this paper, we assume a standard flat  $\Lambda$ CDM cosmology with parameters  $H_0 = 70 \text{ km s}^{-1} \text{ Mpc}^{-1}$ ,  $\Omega_m = 0.3$  and  $\Omega_\Lambda = 0.7$ .

## 2. Observations and data

### 2.1 MUSE spectroscopic data

The MAGPI survey<sup>1</sup> is an ongoing Large Program on the VLT/MUSE, targeting 56 fields from the Galaxy and Mass Assembly (GAMA; Driver et al., 2011) G12, G15 and G23 fields. MAGPI also includes archival observations of legacy fields Abell 370 and Abell 2744. The survey targets a total of 60 primary galaxies with stellar masses  $M_* > 7 \times 10^{10} M_\odot$  and  $\sim 100$  satellite galaxies with  $M_* > 10^9 M_\odot$ . The primary objective of MAGPI is to conduct a detailed spatially resolved spectroscopic analysis of stars and ionized gas within  $0.25 < z < 0.35$  galaxies (see Foster et al., 2021). Data are taken using the MUSE Wide Field Mode ( $1' \times 1'$ ) with a spatial sampling rate of  $0.2''/\text{pixel}$  and the median Full Width at Half Maximum (FWHM) is  $0.64''$  in  $g$  band,  $0.6''$  in  $r$  band and  $0.55''$  in  $i$  band. Each field is observed in six observing blocks, each comprising  $2 \times 1320 \text{ s}$  exposures, resulting in a total integration time of 4.4 h. The survey primarily employs the nominal mode, providing a wavelength coverage ranging from  $4700 \text{ \AA}$  to  $9350 \text{ \AA}$ , with a dispersion of  $1.25 \text{ \AA}$ . Ground-layer adaptive optics (GLAO) is used to correct atmospheric seeing effects, resulting in a gap between  $5805 \text{ \AA}$  and  $5965 \text{ \AA}$  due to the GALACSI laser notch filter. The depth of MAGPI data allows for the detection of both foreground sources within the Local Universe and distant background sources, including LAEs at  $2.9 \lesssim z \lesssim 6.6$ .

The raw MUSE data cubes are reduced using `pymusepipe2`<sup>2</sup>, a Python wrapper for the ESO MUSE reduction pipeline (Weilbacher et al., 2020). This pipeline is used to perform the standard bias and overscan subtraction, flat-fielding, wavelength

calibration and telluric correction. Additional information about the data reduction process is provided in Foster et al. (2021) and it will be presented in a greater detail (Mendel et al. in prep.). LSDCat<sup>3</sup> (Herenz & Wisotzki, 2017) was used for the identification of faint sources — particularly LAEs — accompanied by both automated and visual inspection. LAEs are confirmed using visual inspections of line-profiles and using MARZ<sup>4</sup> redshifting software (Hinton et al., 2016) to rule out interlopers. This search led to the detection of 380 new LAEs distributed across 35 MAGPI fields (Mukherjee et al. in prep). Among these, we found 22 LAEs with  $\log(L_{\text{Ly}\alpha} [\text{erg s}^{-1}]) > 42.4$  at  $5.5 \lesssim z \lesssim 6.6$ .

**Table 1.** HSC photometry of MAGPI LAEs at  $z = 5.5 - 6.6$ , in order of increasing redshift. HSC- $i$ ,  $z$  and  $\gamma$  band AB magnitudes and  $2\sigma$  limits (for non-detections) are presented.  $M_{\text{UV}}$  is the rest-frame absolute UV magnitude estimated from the  $\gamma$ -band magnitudes.

MAGPI ID	HSC- $i$	HSC- $z$	HSC- $\gamma$	$M_{\text{UV}}$
1507091138	$25.52 \pm 0.12$	$25.10 \pm 0.18$	$24.43 \pm 0.19$	$-22.20$
1527275156	$25.29 \pm 0.13$	$25.34 \pm 0.29$	$24.46 \pm 0.21$	$-22.17$
2310233132	–	–	–	–
1527283124	$26.21 \pm 0.33$	$26.10 \pm 0.45$	$26.66 \pm 1.08$	$-19.96$
1503111271	$26.04 \pm 0.24$	$26.86 \pm 0.91$	$25.82 \pm 0.86$	$-20.80$
1507313178	$> 27.18$	$> 26.86$	$> 25.75$	$> -20.87$
1511268137	$> 27.55$	$> 27.49$	$> 26.21$	$> -20.41$
1207184066	–	–	–	–
2306257117	–	–	–	–
1205187075	$> 28.25$	$> 29$	$> 26.40$	$> -20.22$
1523134187	$25.59 \pm 0.19$	$24.39 \pm 0.32$	$24.31 \pm 0.33$	$-22.30$
1507308274	$> 29$	$> 27.37$	$> 25.19$	$> -21.42$
2310245276	–	–	–	–
1204117107	$26.82 \pm 0.49$	$25.26 \pm 0.25$	$24.33 \pm 0.19$	$-22.28$
1529110045	$25.74 \pm 0.13$	$25.26 \pm 0.16$	$25.60 \pm 0.40$	$-21.01$
1529106057	$25.93 \pm 0.23$	$24.49 \pm 0.16$	$25.06 \pm 0.35$	$-21.55$
2310222098	–	–	–	–
1528094186	$26.72 \pm 0.42$	$< 27.61$	$25.38 \pm 0.5$	$-21.22$
1505103163	$25.85 \pm 0.25$	$25.84 \pm 0.56$	$23.32 \pm 0.30$	$-23.27$
1530068179	$> 26.17$	$> 27$	$> 26.85$	$> -19.74$
1528263095	$> 26.13$	$> 27.44$	$> 26.46$	$> -20.12$
1522272275	$25.87 \pm 0.22$	$27.05 \pm 1.01$	$25.25 \pm 0.41$	$-21.33$

### 2.2 HSC photometry

We use optical photometric data for 17 MAGPI LAEs of our sample that are covered in the broad-band filters ( $g$ ,  $r$ ,  $i$ ,  $z$  and  $\gamma$ ) of Subaru HSC Wide layer. HSC Strategic Program (see Aihara et al., 2018) is a wide-field optical imaging survey on the 8.2 meter Subaru Telescope. The HSC-Wide layer data cover about  $300 \text{ deg}^2$  in all five broad-band filters to the nominal survey exposure (10 min in  $g$  and  $r$  bands and 20 min in  $i$ ,  $z$ , and  $\gamma$  bands; see Aihara et al. 2019) with a median seeing  $0.6''$  in the  $i$ -band.

<sup>1</sup>Based on observations obtained using MUSE instrument at VLT of the European Southern Observatory (ESO), Paranal, Chile (ESO program ID 1104.B-0536)

<sup>2</sup><https://github.com/emsellem/pymusepipe>

<sup>3</sup><https://bitbucket.org/Knuser2000/lscat>

<sup>4</sup><https://github.com/Samreay/MarZ>

**Table 2.** Properties of 22 MAGPI LAEs at  $5.5 \lesssim z \lesssim 6.6$  in the sample, in order of increasing redshift. Columns are as follows: MAGPI ID; RA: Right Ascension in degrees; DEC: Declination in degrees;  $z$ : Redshift based on the peak of the Ly $\alpha$  line;  $\log_{10}(L_{\text{Ly}\alpha})$ : observed Ly $\alpha$  luminosity in  $\text{erg s}^{-1}$ ; FWHM: Ly $\alpha$  line width measured using asymmetric Gaussian fit;  $f_{\text{Ly}\alpha}^{\text{cont}}$  \*: Observed UV-continuum flux-density at the location of Ly $\alpha$  wavelength, in  $10^{-20} \text{ erg s}^{-1} \text{ cm}^{-2} \text{ \AA}^{-1}$ ;  $\text{EW}_0$ : Spectroscopically measured Ly $\alpha$  rest-frame equivalent width;  $f_{\text{esc}}^{\text{Ly}\alpha}$ : Ly $\alpha$  escape fraction;  $\log(\xi_{\text{ion}})$ : Ionizing photon production efficiency in  $\text{Hz erg}^{-1}$ ;  $R_{\text{B}}$ : radius of bubble ionized by LAE itself, in pMpc.

MAGPI ID	RA [deg]	DEC [deg]	$z$	$\log_{10}(L_{\text{Ly}\alpha})$ [ $\text{erg s}^{-1}$ ]	FWHM [ $\text{km s}^{-1}$ ]	$f_{\text{Ly}\alpha}^{\text{cont}}$ *	$\text{EW}_0$ [ $\text{\AA}$ ]	$f_{\text{esc}}^{\text{Ly}\alpha}$	$\log(\xi_{\text{ion}})$ [ $\text{Hz erg}^{-1}$ ]	$R_{\text{B}}$ [pMpc]
1507091138	215.6265	0.4041	5.4955	42.77 $\pm$ 0.04	235.45 $\pm$ 24.65	12.09	23.18 $\pm$ 3.28	0.087 <sup>+0.019</sup> <sub>-0.017</sub>	25.26 $\pm$ 0.03	0.55 $\pm$ 0.02
1527275156	220.0398	-0.6588	5.5010	43.50 $\pm$ 0.01	274.29 $\pm$ 8.56	19.89	72.24 $\pm$ 9.65	0.273 <sup>+0.060</sup> <sub>-0.054</sub>	25.51 $\pm$ 0.01	0.66 $\pm$ 0.04
2310233132	348.3007	-34.0181	5.5267	42.76 $\pm$ 0.03	240.43 $\pm$ 15.01	4.05	66.27 $\pm$ 12.43	0.251 <sup>+0.070</sup> <sub>-0.062</sub>	–	0.38 $\pm$ 0.03
1527283124	220.0399	-0.6613	5.5393	42.98 $\pm$ 0.04	211.52 $\pm$ 17.15	6.28	70.2 $\pm$ 17.91	0.266 <sup>+0.094</sup> <sub>-0.083</sub>	25.88 $\pm$ 0.34	0.44 $\pm$ 0.05
1503111271	213.6237	-0.4111	5.6483	42.97 $\pm$ 0.03	252.83 $\pm$ 27.29	20.88	19.74 $\pm$ 4.71	0.074 <sup>+0.024</sup> <sub>-0.021</sub>	26.08 $\pm$ 0.26	0.65 $\pm$ 0.07
1507313178	215.6141	0.4064	5.6570	42.87 $\pm$ 0.03	272.68 $\pm$ 15.15	9.45	34.50 $\pm$ 7.16	0.130 <sup>+0.039</sup> <sub>-0.034</sub>	< 25.72	0.51 $\pm$ 0.04
1511268137	216.5675	1.7274	5.7198	42.55 $\pm$ 0.05	175.55 $\pm$ 17.04	2.17	69.01 $\pm$ 37.78	0.261 <sup>+0.175</sup> <sub>-0.152</sub>	< 25.28	0.31 $\pm$ 0.09
1207184066	182.0006	-2.4909	5.7643	42.40 $\pm$ 0.04	295.35 $\pm$ 32.29	3.27	29.36 $\pm$ 8.73	0.110 <sup>+0.043</sup> <sub>-0.038</sub>	–	0.37 $\pm$ 0.04
2306257117	345.0617	-34.4722	5.7750	42.40 $\pm$ 0.06	213.43 $\pm$ 17.21	4.09	25.40 $\pm$ 8.09	0.095 <sup>+0.040</sup> <sub>-0.035</sub>	–	0.38 $\pm$ 0.05
1205187075	178.0804	-0.8336	5.8010	42.47 $\pm$ 0.05	266.47 $\pm$ 46.14	3.22	37.10 $\pm$ 15.06	0.140 <sup>+0.074</sup> <sub>-0.065</sub>	< 25.54	0.36 $\pm$ 0.06
1523134187	219.5444	-1.0999	5.9285	42.65 $\pm$ 0.03	237.48 $\pm$ 34.83	3.77	42.10 $\pm$ 14.68	0.158 <sup>+0.072</sup> <sub>-0.063</sub>	24.84 $\pm$ 0.01	0.39 $\pm$ 0.06
1507308274	215.6144	0.4117	5.9815	42.73 $\pm$ 0.03	256.93 $\pm$ 33.13	19.36	10.06 $\pm$ 1.59	0.037 <sup>+0.008</sup> <sub>-0.007</sub>	< 25.90	0.66 $\pm$ 0.03
2310245276	348.2999	-34.0101	6.0390	42.52 $\pm$ 0.04	199.64 $\pm$ 20.64	4.96	23.54 $\pm$ 6.15	0.088 <sup>+0.031</sup> <sub>-0.027</sub>	–	0.39 $\pm$ 0.07
1204117107	175.6656	-0.79936	6.0460	43.18 $\pm$ 0.02	367.48 $\pm$ 25.83	35.76	12.50 $\pm$ 3.15	0.046 <sup>+0.016</sup> <sub>-0.014</sub>	25.91 $\pm$ 0.03	0.86 $\pm$ 0.09
1529110045	220.3717	-0.1079	6.0462	42.93 $\pm$ 0.03	197.49 $\pm$ 18.16	8.11	43.2 $\pm$ 13.37	0.163 <sup>+0.067</sup> <sub>-0.059</sub>	25.62 $\pm$ 0.06	0.47 $\pm$ 0.06
1529106057	220.3720	-0.1072	6.0464	43.27 $\pm$ 0.01	262.15 $\pm$ 21.19	18.08	38.92 $\pm$ 7.83	0.147 <sup>+0.043</sup> <sub>-0.038</sub>	25.79 $\pm$ 0.04	0.63 $\pm$ 0.06
2310222098	348.3013	-34.0200	6.1485	43.40 $\pm$ 0.01	329.61 $\pm$ 20.75	11.07	65.81 $\pm$ 9.58	0.241 <sup>+0.057</sup> <sub>-0.052</sub>	–	0.59 $\pm$ 0.05
1528094186	219.5400	-1.1004	6.1662	42.78 $\pm$ 0.04	230.72 $\pm$ 26.26	15.77	12.65 $\pm$ 4.23	0.047 <sup>+0.020</sup> <sub>-0.018</sub>	25.83 $\pm$ 0.18	0.57 $\pm$ 0.05
1505103163	214.6632	-1.7198	6.2481	42.72 $\pm$ 0.05	221.43 $\pm$ 47.02	12.26	13.73 $\pm$ 2.55	0.051 <sup>+0.014</sup> <sub>-0.012</sub>	25.01 $\pm$ 0.01	0.57 $\pm$ 0.03
1530068179	222.1510	2.9404	6.4202	42.80 $\pm$ 0.04	247.26 $\pm$ 20.11	4.97	37.43 $\pm$ 12.97	0.141 <sup>+0.063</sup> <sub>-0.056</sub>	< 26.06	0.42 $\pm$ 0.06
1528263095	220.2286	-1.6538	6.5540	42.57 $\pm$ 0.06	163.44 $\pm$ 21.19	6.53	16.83 $\pm$ 4.77	0.063 <sup>+0.024</sup> <sub>-0.021</sub>	< 26.03	0.45 $\pm$ 0.04
1522272275	219.0635	0.8046	6.6073	43.32 $\pm$ 0.02	325.20 $\pm$ 20.33	32.84	16.97 $\pm$ 3.57	0.063 <sup>+0.019</sup> <sub>-0.017</sub>	26.29 $\pm$ 0.08	0.80 $\pm$ 0.07

Using HSC command-line SQL (Structured Query Language) tool <sup>5</sup>, we retrieve the Wide layer photometric data from data-release 2 (Aihara *et al.*, 2019). We extract fluxes and corresponding  $1\sigma$  flux uncertainties and limiting  $2\sigma$  fluxes (for non-detections) using  $2''$  aperture diameter. These fluxes and corresponding uncertainties for  $i$ ,  $z$  and  $y$  bands are presented in Table 1.

### 3. Data analyses

For our sample of 22 LAEs, 1D spectra are extracted using an aperture of  $2''$  radius. MUSE 1D spectra reveal the detection of Ly $\alpha$  emissions where spectroscopic redshifts are determined based on the peak of the Ly $\alpha$  line. No other associated emission lines are found in the MUSE data for these 22 LAEs, restricting the measurement of systemic redshift. Below we estimate UV magnitudes and discuss the procedures of analysing Ly $\alpha$  spectra to study properties of these LAEs.

#### 3.1 Estimating UV magnitudes

Out of the 22 sources, 11 LAEs are detected in HSC broadband filters. HSC does not cover GAMA23 fields and hence

we do not have photometric data for four sources in this field. We also do not have photometric data for MAGPI1207184066 as it is located at the edge of the HSC field. For rest of the six sources, which are not detected in HSC, we calculate a  $2\sigma$  limit on the magnitudes (see Table 1). As we do not have photometry beyond  $y$  band, no meaningful constraints can be obtained on the UV slope ( $\beta$ ). Therefore, we assume a flat UV slope  $\beta = -2$ , which is the typical value that most of the high-redshift galaxies have (see, Dunlop *et al.*, 2013; Bouwens *et al.*, 2014; Matthee *et al.*, 2017b). We convert the  $y$  band magnitudes to the rest-frame absolute UV magnitudes ( $M_{\text{UV}}$ ) at 1500  $\text{\AA}$ . We also note that, for  $z > 6$  sources,  $y$ -band magnitude is not exactly measuring the flux at 1500  $\text{\AA}$ . Still, it provides a decent approximation of the UV magnitudes. The estimated UV magnitudes of our sources lie in the range  $-19.74 \lesssim M_{\text{UV}} \lesssim -23.27$ , which are given in Table 1.

#### 3.2 Line profile fitting

We use `pyplatefit` <sup>6</sup>, a python module (Bacon *et al.*, 2023) to fit a local continuum and obtain a continuum subtracted spectrum. `pyplatefit` performs a continuum fit around the

<sup>5</sup><https://hsc-release.mtk.nao.ac.jp/datasearch>

<sup>6</sup><https://github.com/musevlt/pyplatefit>

observed Ly $\alpha$  line in a spectral window of  $\pm 50$  Å centred on the Ly $\alpha$  line, using a simple stellar population model (Bruzual & Charlot, 2003). It then subtracts the continuum and returns a continuum-subtracted spectrum. Next we fit the continuum-subtracted Ly $\alpha$  profiles using an asymmetric Gaussian which has been found to provide an extremely good representation of the Ly $\alpha$  line (see Shibuya et al., 2014; Herenz et al., 2017; Claeysens et al., 2019; Songaila et al., 2024):

$$F(\lambda) = f_{\max} \exp\left(-\frac{\Delta\nu^2}{2(a_{\text{asym}}(\Delta\nu) + w)^2}\right) \quad (1)$$

where  $f_{\max}$  is the flux normalization (amplitude),  $\Delta\nu$  is the velocity shift (in km s $^{-1}$ ) relative to the peak velocity,  $a_{\text{asym}}$  determines the asymmetry or skewness of the line and  $w$  (in km s $^{-1}$ ) controls the line width (FWHM). A positive asymmetry value suggests that the Ly $\alpha$  line has a red wing, which is usually seen in most of the single-peaked Ly $\alpha$  lines (Kerutt et al., 2022; Songaila et al., 2022). The line width can be obtained in terms of fitting parameters as follows (see also, Claeysens et al., 2019; Songaila et al., 2024):

$$\text{FWHM (km s}^{-1}\text{)} = \frac{2\sqrt{2\ln(2)} w}{(1 - 2\ln(2) a_{\text{asym}}^2)} \quad (2)$$

The corresponding error in the FWHM is almost fully dominated by the error in  $w$ , with only a few percent contribution from the asymmetry term. The fits on the continuum-subtracted spectra along with the values of the free parameters and corresponding 1 $\sigma$  errors are shown in Appendix 1.

### 3.3 Spectroscopic measurements

Using a single asymmetric Gaussian fit to the Ly $\alpha$  profile extracted using 2'' radius aperture, as mentioned above, we measure Ly $\alpha$  line fluxes ( $F_{\text{Ly}\alpha}$ ) for our LAEs. In Fig. 1, we compare them with the 3  $R_{\text{KRON}}$  fluxes obtained using LSDCat (flux extracted using the aperture of radius  $3 \times R_{\text{KRON}}$  that contains > 95% of the total line flux; (see, Graham & Driver, 2005; Herenz et al., 2017). The values of 3  $R_{\text{KRON}}$  radii in which fluxes were extracted are ranging from 1.6'' to 2.2''. Since both flux values match well, we conclude that our line flux measurements are accurate. The observed Ly $\alpha$  luminosities ( $L_{\text{Ly}\alpha}$ ) are then calculated from fluxes as  $L_{\text{Ly}\alpha} = 4\pi F_{\text{Ly}\alpha} D_L^2$ , where  $D_L$  is the luminosity distance, calculated using the cosmological parameters that we assume in §1.

We measure the Ly $\alpha$  EW $_0$  to investigate the strength of the Ly $\alpha$  line. In order to do that, we need measurements of UV continuum flux density at the Ly $\alpha$  wavelength. However, due to lack of UV-slope measurement (see §3.1), it is not possible to determine continuum flux density from the photometric data. Further, Hashimoto et al. (2017) caution that fixing the value of UV-slope  $\beta$  at high-redshift can lead to an underestimation of EW $_0$  due to the redshift evolution of  $\beta$ . Therefore, we obtain the observed median UV-continuum flux density ( $f_{\text{Ly}\alpha}^{\text{cont}}$ ) from the continuum fit performed using `pyplatefit` (see §3.2). We then divide the total Ly $\alpha$  line

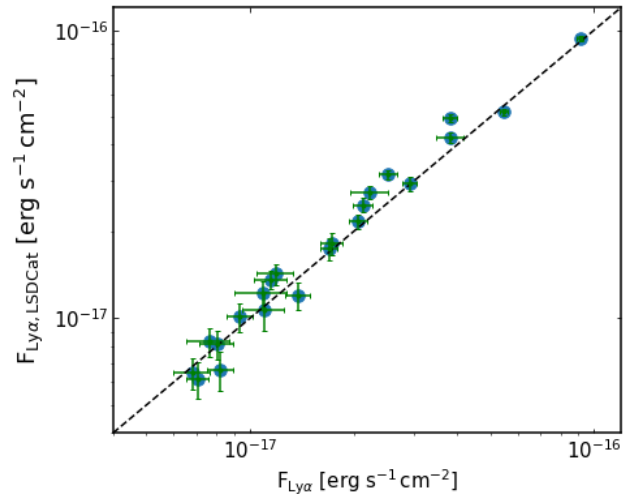


**Figure 1.** Ly $\alpha$  line fluxes obtained from MUSE 1D spectra (extracted using 2'' radius aperture) are compared against LSDCat 3  $R_{\text{KRON}}$  fluxes. The one-to-one relation is shown as the dashed line.

flux ( $F_{\text{Ly}\alpha}$ ) by  $f_{\text{Ly}\alpha}^{\text{cont}}$  to determine observed Ly $\alpha$  equivalent width (EW). The rest-frame equivalent width is then given as  $\text{EW}_0 = \text{EW}/(1+z)$ . We note that for some LAEs, the continuum in the MUSE data is too faint, and thus we can only derive lower limits for EW $_0$  for them. As H $\alpha$  emission is not covered within the MUSE spectral range, Ly $\alpha$  escape fraction can not be directly measured. A strong correlation between  $f_{\text{esc}}^{\text{Ly}\alpha}$  and EW $_0$  has been found in both low- and high-redshift LAEs (see, Matthee et al., 2017b; Yang et al., 2017; Sobral & Matthee, 2019; Begley et al., 2024). In Begley et al. (2024), a sample of 152 star-forming galaxies with  $z \sim 4-5$  is used to obtain a linear dependence between  $f_{\text{esc}}^{\text{Ly}\alpha}$  and EW $_0$ . We estimate  $f_{\text{esc}}^{\text{Ly}\alpha}$  using this best-fit relation. We tabulate the spectroscopic properties of these LAEs in Table 2.

Begley et al. (2024) discuss that their  $f_{\text{esc}}^{\text{Ly}\alpha}$  - EW $_0$  relation agrees well with the relation derived for low-redshift LAEs (Sobral & Matthee, 2019). The observed scatter in this relation are found to be well-consistent with that observed in both low and high- $z$  LAE samples (see, Pucha et al., 2022; Roy et al., 2023). A similar positive correlation has also been observed in LAEs in the reionization era (Saxena et al., 2024; Tang et al., 2024b). However, the slope, normalization and scatter of the observed  $f_{\text{esc}}^{\text{Ly}\alpha}$  - EW $_0$  relationship are likely influenced by dust attenuation, differential dust geometry and  $\xi_{\text{ion}}$  (Matthee et al., 2017a; Harikane et al., 2018; Shivaie et al., 2018; Sobral & Matthee, 2019). Additionally, for a given EW $_0$  value, intrinsic scatter in  $f_{\text{esc}}^{\text{Ly}\alpha}$  is expected due to variations in stellar populations and dust/gas properties (Begley et al., 2024). We conclude that, despite the complexity of factors,  $f_{\text{esc}}^{\text{Ly}\alpha}$  can be predicted within  $\sim 0.5$  dex of actual values from the  $f_{\text{esc}}^{\text{Ly}\alpha}$  - EW $_0$  relation of Begley et al. (2024) using only the equivalent width information.

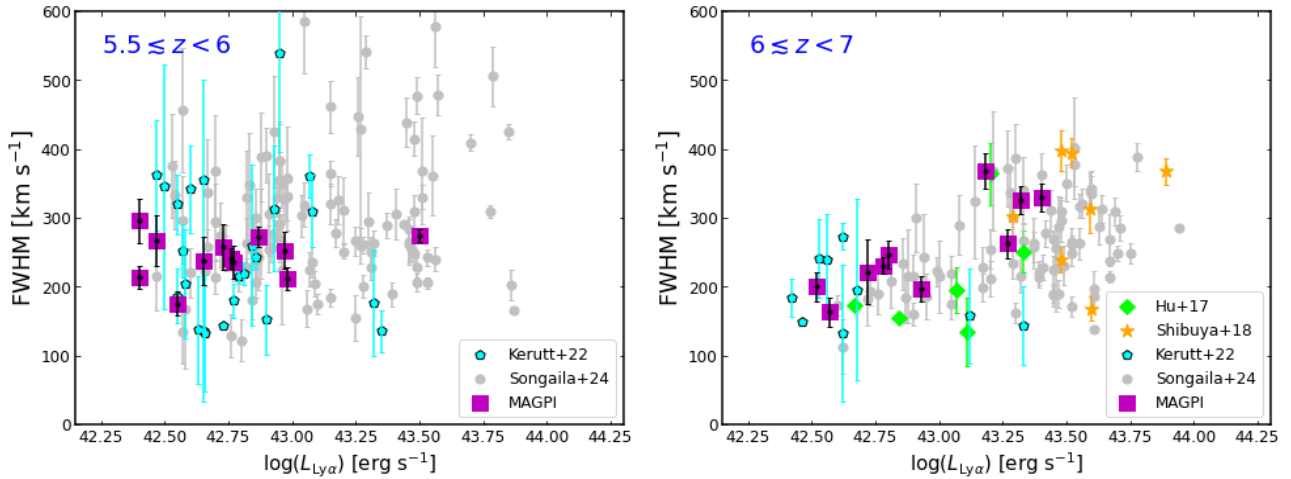


**Figure 2.** Evolution of Ly $\alpha$  line width is shown as function of Ly $\alpha$  luminosity at  $5.5 \lesssim z < 6$  (left panel) and at  $6 \lesssim z < 7$  (right panel). MAGPI LAEs (this work) are shown as purple squares. We also include data from MUSE DEEP and MUSE WIDE surveys (blue pentagons; Kerutt et al., 2022), (grey circles; Songaila et al., 2024), LAGER survey (green diamonds; Hu et al., 2017) and (orange stars; Shibuya et al., 2018).

## 4. Results and discussions

We present photometric and spectroscopic properties (see Table 1 and Table 2 respectively) of 22 LAEs at  $5.5 \lesssim z \lesssim 6.6$ . These sources have Ly $\alpha$  luminosities  $\log(L_{\text{Ly}\alpha} [\text{erg s}^{-1}]) = 42.4\text{--}43.5$  and Ly $\alpha$  rest-frame equivalent widths  $\text{EW}_0 \simeq 10\text{--}72 \text{ \AA}$ . In the following subsections, we explore the relation between the Ly $\alpha$  line width and Ly $\alpha$  luminosity and investigate this relation in the context of the size of the ionized bubbles created by each LAE at the end of the reionization era.

### 4.1 Evolution of the Ly $\alpha$ line width

We fit the Ly $\alpha$  lines with an asymmetric/skewed Gaussian. This provides excellent representation of all the Ly $\alpha$  profiles. All of the asymmetry parameters are positive, corresponding to red-skewed profiles. The asymmetry of all the lines also confirm that these are Ly $\alpha$  emission from star-forming galaxies rather than other emission lines from low-redshift interlopers. In Fig. 2, we present the evolution of Ly $\alpha$  line widths with Ly $\alpha$  luminosities across two redshifts ranges. For MAGPI LAEs, we find that at  $z < 6$  (see Fig 2, left panel), FWHM distribution is almost uniform, with no significant evolution with increasing luminosities. In contrast,  $z > 6$  LAEs show a strong evolution of increasing line width with increasing luminosities (see Fig. 2, right panel). For comparison, we also include data from MUSE DEEP and MUSE WIDE surveys (Kerutt et al., 2022), bright LAEs from Shibuya et al. (2018),  $z \sim 6.9$  LAEs from LAGER survey (Hu et al., 2017) and recent large sample of LAEs from Songaila et al. (2024), which allows a better understanding of the evolution of line widths across a wide redshift range ( $5.5 \lesssim z \lesssim 7$ ) at the edge of reionization. We note large uncertainties in luminosities and FWHMs in the data of Kerutt et al. (2022). Apart from that, we find our result is well-consistent with the others. We note that, at  $z > 6$ , line widths of MAGPI LAEs are narrower ( $\text{FWHM} \lesssim 250 \text{ km s}^{-1}$ ) at luminosities  $\log(L_{\text{Ly}\alpha} [\text{erg s}^{-1}]) < 43$ , as compared to LAEs at  $\log(L_{\text{Ly}\alpha} [\text{erg s}^{-1}]) > 43$ , where we find broader line widths

(i.e.  $\text{FWHM} > 260 \text{ km s}^{-1}$ ). The visibility of Ly $\alpha$  emission from high-redshift star-forming galaxies is primarily determined by the star formation rate and ionizing photon budget, which influence the size of ionized bubbles around them that allow Ly $\alpha$  photons to travel unattenuated along the line of sight (Malhotra & Rhoads, 2006). Despite the fact that increasingly neutral IGM potentially scatters most of the Ly $\alpha$  photons and make the line narrower, the broadening of the line at  $z > 6$  suggests that the high-luminosity LAEs may preferentially lie in more highly ionized regions than the lower luminosity LAEs (Matthee et al., 2017b; Songaila et al., 2024), protecting themselves from the scattering effects of the IGM. In the next section, we discuss how LAEs themselves can produce ionized bubbles around them.

### 4.2 Ionizing photon escape and size of ionized region

The absorption of ionizing photons by the interstellar medium within galaxies leads to Ly $\alpha$  emissions through recombination processes, while photons that escape contribute to cosmic reionization. The size of the ionized region (H II bubble) around an ionizing source can be estimated by solving the evolution equation of the ionizing front (e.g. Cen & Haiman, 2000; Yajima et al., 2018) :

$$\frac{dR_B^3}{dt} = 3H(z)R_B^3 + \frac{3Q_{\text{ion}}f_{\text{esc}}^{\text{LyC}}}{4\pi n_{\text{H}}(z)} - C_{\text{HII}}n_{\text{H}}(z)\alpha_{\text{rec}}R_B^3 \quad (3)$$

where  $R_B$  is the proper physical radius of ionized bubble in physical Mpc (pMpc),  $H(z)$  is the Hubble parameter,  $Q_{\text{ion}}$  is the intrinsic production rate of ionizing photons (in  $\text{s}^{-1}$ ),  $C_{\text{HII}}$  is the clumping factor of ionized hydrogen and  $\alpha_{\text{rec}}$  is the temperature-dependant total recombination rate coefficient under Case B approximation ( $T = 10^4 \text{ K}$ ,  $n_e = 350 \text{ cm}^{-3}$ ). The mean hydrogen density of the IGM ( $n_{\text{H}}$ ) scales with redshift as follows:  $n_{\text{H}} \approx 8.5 \times 10^{-5} \left(\frac{1+z}{8}\right)^3 \text{ cm}^{-3}$  (see, Mason & Gronke, 2020; Meyer et al., 2021).

We can define ionizing photon production rate ( $Q_{\text{ion}}$ ) in terms of direct Ly $\alpha$  observables (see, [Matthee et al., 2017b](#); [Yajima et al., 2018](#); [Sobral & Matthee, 2019](#); [Matthee et al., 2022](#)):

$$Q_{\text{ion}} [\text{s}^{-1}] = \frac{L_{\text{Ly}\alpha}}{c_{\text{H}\alpha} (1 - f_{\text{esc}}^{\text{LyC}}) \times (8.7 f_{\text{esc}}^{\text{Ly}\alpha})} \quad (4)$$

where  $c_{\text{H}\alpha} = 1.36 \times 10^{-12}$  erg (under case B recombination; [Kennicutt, 1998](#); [Schaerer, 2003](#)). Here, we assume negligible nebular attenuation ([Naidu et al., 2022](#)). A detailed discussion on the role of dust in the context of Ly $\alpha$  and LyC escape can be found in [Kakiichi & Gronke \(2021\)](#). In §3.3, we estimated Ly $\alpha$  escape fractions (within  $\simeq 0.5$  dex) using its linear dependence on  $\text{EW}_0$ . However, this relation can be influenced by dust attenuation and  $\xi_{\text{ion}}$ , as discussed in §3.3. A prominent degeneracy between dust extinction and  $\xi_{\text{ion}}$  has been observed in [Sobral & Matthee \(2019\)](#), where higher dust extinction allows for a lower  $\xi_{\text{ion}}$  and vice versa. Current data restrict us from accurately estimating both  $f_{\text{esc}}^{\text{Ly}\alpha}$  and  $\xi_{\text{ion}}$  as it requires dust-corrected H $\alpha$  luminosity. Direct observations of Balmer decrements and high-excitation UV lines are necessary to further validate and confirm our results.

A correlation between Ly $\alpha$  and LyC escape fractions has been investigated in several observational studies and hydrodynamical simulations ([Verhamme et al., 2017](#); [Chisholm et al., 2018](#); [Flury et al., 2022](#); [Maji et al., 2022](#)). [Begley et al. \(2024\)](#) find a linear dependence between  $f_{\text{esc}}^{\text{LyC}}$  and  $f_{\text{esc}}^{\text{Ly}\alpha}$ . Using this relation, we estimate that our sources have  $f_{\text{esc}}^{\text{LyC}} = 0.5 - 4\%$ . Hydrodynamical and radiative transfer simulations are used to calibrate the same relation ([Maji et al., 2022](#)), using which we get  $f_{\text{esc}}^{\text{LyC}} < 3\%$  for our sources. However, this correlation between Ly $\alpha$  and LyC escape does not seem to work well for LyC leakers at higher redshifts (see, [Kerutt et al., 2024](#)). Kinematics and ISM properties of high-redshift leakers are more complex ([Guaita et al., 2015](#)) as compared to low-redshift leakers. A spatial offset between Ly $\alpha$  and LyC emission has been observed in high-redshift leakers ([Kerutt et al., 2024](#); [Gupta et al., 2024](#)), which indicates that the two are escaping from different locations in the galaxy. For instance, high-redshift leakers prefer asymmetric escape (indicating scattering or expanding gas) rather than through optically thin ionized channel, which seems to be the case for low-redshift leakers ([Kerutt et al., 2024](#)).

We do not expect LAEs in our sample to be strong LyC leakers. Hence, we simply assume a fiducial value of LyC escape  $f_{\text{esc}}^{\text{LyC}} = 5\%$  for our sources throughout the analysis. The ionizing photon production efficiency is defined as the ratio of  $Q_{\text{ion}}$  and intrinsic UV luminosity density ( $L_{\text{UV},\nu}$ ) ([Matthee et al., 2017b](#)):

$$\xi_{\text{ion}} [\text{Hz erg}^{-1}] = \frac{Q_{\text{ion}}}{L_{\text{UV},\nu}} \quad (5)$$

We obtain  $L_{\text{UV},\nu}$  from  $M_{\text{UV}}$ , assuming negligible dust attenuation. We refer to [Bouwens et al. \(2016\)](#) for a discus-

sion on the impact of dust attenuation on  $\xi_{\text{ion}}$ . Our measured  $M_{\text{UV}}$  values (see Table 1) indicate that these LAEs are UV-bright ( $-19.74 \leq M_{\text{UV}} \leq -23.27$ ). The estimated  $\xi_{\text{ion}}$  values are presented in Table 2. For the sources, which are detected in HSC, we find an average ionizing photon production efficiency  $\log(\xi_{\text{ion}} [\text{Hz erg}^{-1}]) = 25.51$  at  $z < 6$ , while  $\log(\xi_{\text{ion}} [\text{Hz erg}^{-1}]) = 25.74$  at  $z > 6$ . The slight evolution of  $\xi_{\text{ion}}$  with redshift is consistent with the previous studies (eg. [Bouwens et al., 2014](#); [Endsley et al., 2021b](#); [Simmonds et al., 2023](#); [Tang et al., 2023](#); [Saxena et al., 2024](#)). This aligns with the idea that younger galaxies may achieve higher ionizing photon production efficiencies. However, the evolution is very mild which could suggest that the production and escape of ionizing photons are governed by physical processes operating on much shorter timescales, such as intense star formation or supernova activity, which do not show a strong trend with redshift ([Saxena et al., 2024](#)). Further, we also note that some of the low-equivalent width (therefore, low  $f_{\text{esc}}^{\text{Ly}\alpha}$ ) LAEs ( $\text{EW}_0 < 20 \text{ \AA}$ ; i.e, MAGPI1503111271, MAGPI1204117107, MAGPI1528094186, and MAGPI1522272275) show higher  $\xi_{\text{ion}}$  (see Table 2). Such a tentative anti-correlation between  $f_{\text{esc}}^{\text{Ly}\alpha}$  and  $\xi_{\text{ion}}$  has been reported in a large sample of LAEs from JEMS and MUSE (see [Simmonds et al., 2023](#)). This could indicate a time delay between production and escape of ionizing photons in these galaxies ([Katz et al., 2020](#)), which again may be linked to supernova activity.

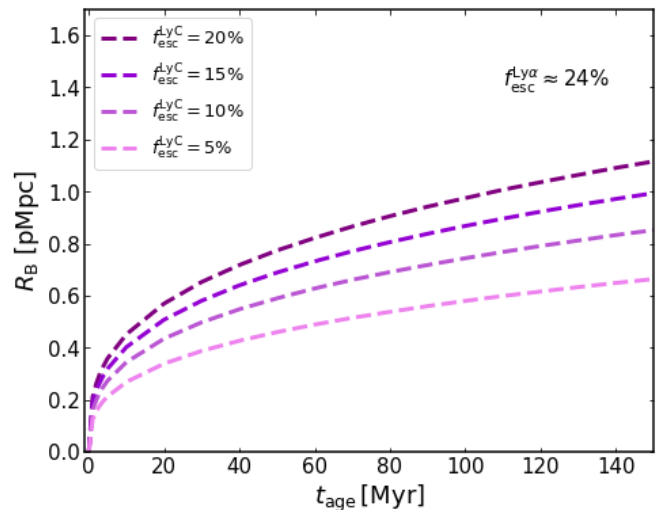


**Figure 3.** Radius of spherical bubble ionized by MAGPI2310222098 as a function of the age parameter ( $t_{\text{age}}$ ), for different values of the LyC escape fraction ( $f_{\text{esc}}^{\text{LyC}} = 5\%$ ,  $10\%$ ,  $15\%$  and  $20\%$ ). Here we assume a fixed Ly $\alpha$  escape fraction  $f_{\text{esc}}^{\text{Ly}\alpha} = 24\%$ , as estimated (see Table 2).

For constant Ly $\alpha$  luminosity and  $f_{\text{esc}}^{\text{LyC}}$ , hence for a constant production rate  $Q_{\text{ion}}$ , Eq. (3) can be solved analytically to obtain an expression of bubble sizes that can be produced by the LAE on its own. For instance, neglecting the accelerated expansion due to Hubble flow and for luminous sources at  $z \lesssim 8$ , when the recombination rate is relatively low, second term of Eq. (3) dominates and we get an expression for bubble

radius (Cen & Haiman, 2000):

$$R_B \approx \left( \frac{3 Q_{\text{ion}} f_{\text{esc}}^{\text{LyC}} t_{\text{age}}}{4\pi n_{\text{H}}(z)} \right)^{1/3} \quad (6)$$

where  $t_{\text{age}}$  is the time since the ionizing source has switched on. For these estimates, we assume a fiducial value of  $t_{\text{age}} = 100$  Myr (a reasonable amount of time for  $f_{\text{esc}}^{\text{LyC}} = 5\%$ ; see Wistok *et al.*, 2024; Whitler *et al.*, 2024) for all the LAEs. Recent studies note that the inferred bubble size does not strongly depend on small deviations in LyC escape fraction and age (see, Wistok *et al.*, 2024; Torralba-Torregrosa *et al.*, 2024). For one luminous LAE (ID: MAGPI2310222098), we study the evolution of bubble size as a function of  $t_{\text{age}}$  for different values of the LyC escape fraction (see, Fig. 3). For a constant Ly $\alpha$  escape fraction ( $f_{\text{esc}}^{\text{Ly}\alpha} \approx 24\%$ ), we find that this LAE is capable of ionizing a bubble of radius  $R_B \sim 0.59$  pMpc in  $t_{\text{age}} = 100$  Myr for a LyC escape of  $f_{\text{esc}}^{\text{LyC}} = 5\%$  while it takes  $t_{\text{age}} = 50$  (30) Myr to ionize the same bubble size, when  $f_{\text{esc}}^{\text{LyC}} = 10$  (15)%. We also note that  $t_{\text{age}}$  depends on the actual time duration of constant star-formation within the galaxy, which is fundamentally bounded to  $\lesssim 200$  Myr at this epoch (see, Tacchella *et al.*, 2018; Whitler *et al.*, 2023).

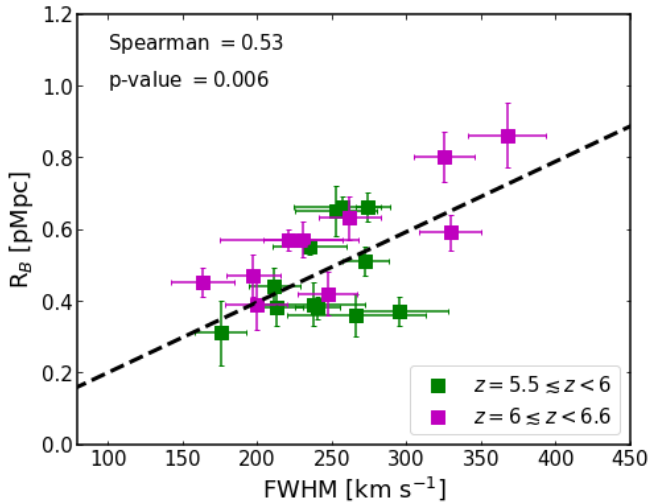


**Figure 4.** Evolution of the bubble radius as a function of Ly $\alpha$  line width for our 22 MAGPI LAEs. LAEs at  $5.5 \lesssim z < 6$  are highlighted in green squares whereas LAEs at  $z > 6$  are shown in purple squares. Significance of the plot (Spearman correlation coefficient and p-value) are shown in the top left corner.

Based on the assumptions mentioned above ( $t_{\text{age}} = 100$  Myr and  $f_{\text{esc}}^{\text{LyC}} = 5\%$ ), we find that each of our LAEs reside in ionized bubbles of radii  $R_B = 0.31 - 0.86$  pMpc (see, Table 2). From Eq. (4) and Eq. (6), we note that bubble radius scales with the Ly $\alpha$  luminosity as  $R_B \propto L_{\text{Ly}\alpha}^{1/3}$ . Modeling of Ly $\alpha$  emission and transmission during the EoR also predicts that Ly $\alpha$  luminosity increases with  $R_B$  due to higher IGM transmission for large ionized bubbles (see, Yajima *et al.*, 2018).

We find a linear correlation between bubble radii and Ly $\alpha$  line widths (see Fig. 4) with high statistical significance (Spearman correlation coefficient = 0.53 and p-value = 0.006). This trend is more prominent in LAEs at  $z > 6$ , which is expected given the correlation between Ly $\alpha$  luminosity and line width at  $z > 6$ , as discussed in the previous section. This again supports the fact that broadening of Ly $\alpha$  lines at  $z > 6$  is due to large ionized bubble which are created around them, allowing most of the Ly $\alpha$  photons to come out of that the galaxy without suffering from much scattering in the IGM (Songaila *et al.*, 2022, 2024).

At high redshifts, Ly $\alpha$  lines are usually redshifted with respect to systemic velocity due to strong outflows, which facilitates the transmission of Ly $\alpha$  photons through IGM (Dijkstra *et al.*, 2011). The velocity offset of the red peak has been used to place lower limits on the bubble sizes required for IGM transmission (Mason & Gronke, 2020; Wistok *et al.*, 2024). Considering a patchy reionization scenario, where a galaxy is typically surrounded by a completely neutral IGM, it is found that Ly $\alpha$  can be detected at a high velocity offset of  $\gtrsim 300$  km s $^{-1}$  when the galaxy is situated in a ionized region of radius  $R_B \gtrsim 0.1$  pMpc (see Mason & Gronke, 2020; Umeda *et al.*, 2023). A Bayesian approach of modeling intrinsic Ly $\alpha$  profiles has predicted the size of ionized regions to be  $R_B = 0.5 - 2.5$  pMpc at  $z > 6$  (Hayes & Scarlata, 2023). Wistok *et al.* (2024) find that LAEs with relatively low Ly $\alpha$  velocity offset ( $\lesssim 300$  km s $^{-1}$ ) with moderately high escape fraction can represent ionized regions of sizes  $R_B = 0.1 - 1$  pMpc. Further, several attempts have been made to put constraints on the size of ionized regions that allow blue peak of Ly $\alpha$  to be detected at  $z > 6$ , where it is found that the blue peak can be detected if the source galaxy resides in a highly ionized region ( $x_{\text{HI}} > 10^{-5}$ ) of radius  $R_B \gtrsim 0.5$  pMpc (see, Mason & Gronke, 2020; Torralba-Torregrosa *et al.*, 2024). We note that, while some of our LAEs show larger bubble sizes, we can not always anticipate seeing a blue-peak emission from them, as these photons might be heavily absorbed by neutral hydrogen in the circumgalactic medium (CGM; Henry *et al.*, 2015; Gazagnes *et al.*, 2020; Endsley & Stark, 2022).

Ly $\alpha$  radiative transfer modeling suggests strong correlation between Ly $\alpha$  velocity offset and  $N_{\text{HI}}$  (Verhamme *et al.*, 2015). As  $N_{\text{HI}}$  increases the peak velocity shifts farther from the systemic velocity. Further, shell model predicts that for a low  $N_{\text{HI}}$  and high outflow velocity, most of the Ly $\alpha$  photons can directly escape at the line centre frequency (Yajima *et al.*, 2018). In addition, line width becomes narrower when  $N_{\text{HI}}$  decreases. This is expected as low  $N_{\text{HI}}$  shifts the peak to shorter wavelengths, where Ly $\alpha$  flux is significantly reduced due to IGM scattering. While IGM radiative transfer establishes a typical correlation between the line width and velocity offset of Ly $\alpha$  red peaks (e.g. Neufeld, 1990; Verhamme *et al.*, 2018; Li & Gronke, 2022), this trend is expected to change at high redshifts due to IGM absorption. Ignoring such complicated radiative transfer effects at high redshifts, we can simply assume that Ly $\alpha$  line width is positively correlated with  $N_{\text{HI}}$  as  $\text{FWHM} \simeq 320 \left( \frac{N_{\text{HI}}}{10^{20} \text{cm}^{-2}} \right)^{1/3}$  (Dijkstra, 2017; Li & Gronke,



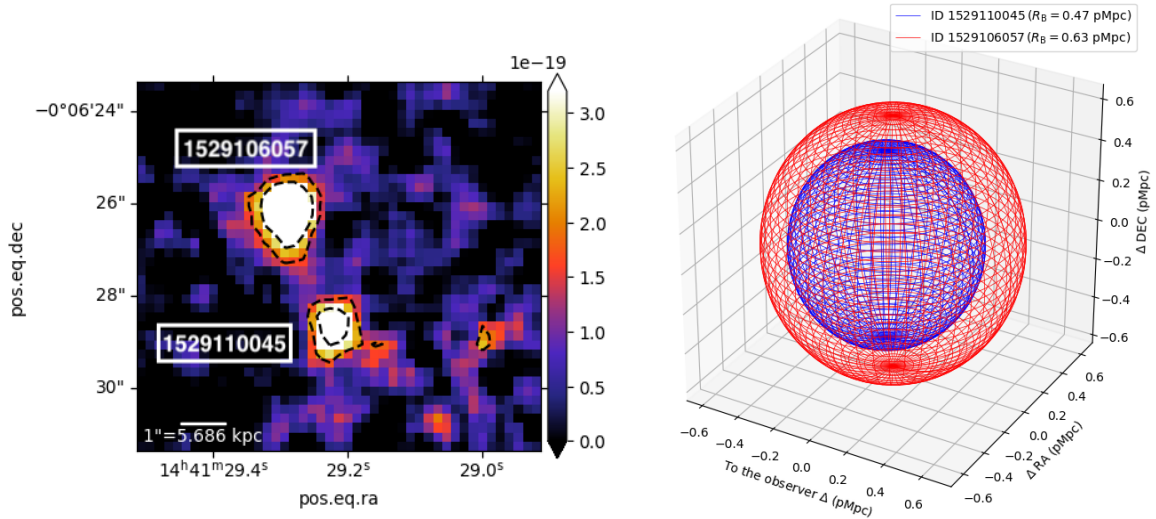


**Figure 5.** *Left panel:* Synthetic MUSE Ly $\alpha$  narrow band (NB) image collapsed for wavelengths within 8550 Å to 8590 Å, showing two LAEs with MAGPI IDs 1529106057 and 1529110045 at  $z = 6.046$ , separated by a physical distance of 15.92 kpc. Contours are shown as black dashed lines at the 2 and 4 $\sigma$  significance levels. *Right panel:* Three-dimensional visualization of the size of ionized bubbles created by them along the line of sight. Bubbles are shown in wire-frame spheres centred on each LAE. The centre of the LAE MAGPI1529110045 is at the origin of this 3D plot.

2022) for a static shell with temperature  $T_{\text{eff}} = 10^4$  K. This translates to a column density  $\log(N_{\text{HI}}) \sim 20.18 \text{ cm}^{-2}$  for the highest FWHM LAE in our sample (i.e. MAGPI1204117107 at  $z = 6.046$ ). Further, using the correlation between velocity offset and  $\log(N_{\text{HI}})$  (which is approximated by a second order polynomial, see Fig. 2 of Verhamme et al., 2015), we expect this line to be at an offset of  $300 \text{ km s}^{-1}$ . We follow the IGM transmission model of Wistok et al. (2024) and find that this LAE can have  $> 30\%$  IGM transmission if it resides inside a bubble of radius  $R_B = 0.86$  pMpc. This estimation is in agreement with the findings of Endsley et al. (2022), where they discover boosted Ly $\alpha$  transmission in LAEs with large velocity offsets and broad line widths. On the other hand, MAGPI2310245276 at  $z = 6.039$  (FWHM =  $199.64 \text{ km s}^{-1}$ ) can only transmit  $< 10\%$  of Ly $\alpha$  photons if it resides in  $R_B = 0.39$  pMpc bubble. However, it is also possible that for a very low velocity offset ( $< 200 \text{ km s}^{-1}$ ), a sufficiently large ( $R_B > 1.5$  pMpc) bubble will be able to transmit  $> 60\%$  of Ly $\alpha$  photons (see, Fig. 3 of Wistok et al., 2024) by reducing the scattering effect, which can increase the observed Ly $\alpha$  luminosity and may allow some photons to escape on the bluer side. A better understanding of  $N_{\text{HI}}$  - FWHM - velocity offset relation at  $z > 6$  will require efficient radiative transfer modeling of these high-redshift LAEs.

Our analysis suggests that galaxies with broader Ly $\alpha$  emission lines are generally located within larger ionized bubbles. However, we caution that this may not always hold true. For instance, UV-bright galaxies in the reionization era may exhibit wider Ly $\alpha$  line profiles if they have more H I present in their CGM, resulting in more scattering of Ly $\alpha$  photons (see, Tang et al., 2023). Moreover, UV-bright galaxies are found to display larger Ly $\alpha$  velocity offsets (e.g. Endsley et al., 2022; Valentino et al., 2022; Tang et al., 2023; Witten et al., 2023). In such cases, most of the Ly $\alpha$  photons emerge at relatively high velocities, experiencing minimal attenuation by the neutral

IGM (see, Mason & Gronke, 2020). Visibility of Ly $\alpha$  during reionization can also be enhanced by efficient ionizing photon production due to hard ionizing field (e.g. Mainali et al., 2018; Tang et al., 2023), or if Ly $\alpha$  is produced in gas clumps moving with large peculiar motions, leading to intrinsically broad Ly $\alpha$  profile (e.g. Endsley et al., 2022). Therefore, wide Ly $\alpha$  lines from LAEs can survive even in moderate-sized ionized bubbles (e.g. Endsley et al., 2022). Future observations of Ly $\alpha$  in both UV-bright and faint galaxies during the reionization era will provide more precise constraints on bubble sizes and the influence of the IGM on Ly $\alpha$  transmission.

#### 4.3 Closely separated LAE pair: overlapping bubbles?

We find two closely separated LAE pairs. There are two LAEs in MAGPI2310 field (MAGPI IDs: 2310245276 and 2310222098) at  $z = 6.039$  and  $z = 6.1485$  respectively, are located  $36''$  apart on the sky, which corresponds to a physical distance of 203 kpc. Their separation along the line of sight is 6.32 pMpc. As a result, the estimated radii of their bubbles indicate that these bubbles do not overlap. We also find two LAEs at  $z = 6.046$  in MAGPI1529 field (MAGPI IDs: 1529106057 and 1529110045), whose redshifts differ only by 0.0002, which corresponds to a velocity shift of only  $61 \text{ km s}^{-1}$ . They are located only  $3''$  apart on the sky (see Fig. 5), translating to a projected physical separation of 15.92 kpc. The estimated bubble radii for them suggest that their bubbles overlap and they likely sit inside a single large ionized region (see Fig. 5, right panel).

Closely separated LAEs have been previously observed in the reionization era (see, Castellano et al., 2016; Hu et al., 2017; Tilvi et al., 2020; Endsley et al., 2021a; Endsley & Stark, 2022; Chen et al., 2024; Wistok et al., 2024). Many of these LAEs are found to reside in overdense regions populated by fainter galaxies (e.g. Castellano et al., 2016, 2018; Chen et al.,

2024; Witstok *et al.*, 2024; Whitler *et al.*, 2024). On the other hand, Endsley & Stark (2022) detect many UV-bright galaxies making an overdense region around three closely-separated Lyman-break galaxies at  $z \sim 6.8$ . Closely separated LAEs in overdense regions can cause bubble overlap, which results in the formation of giant ionized bubbles, allowing a boosted transmission of Ly $\alpha$  through the neutral IGM (Mason *et al.*, 2018; Jung *et al.*, 2022a). With our current data, we can not yet fully characterize the extent of the ionized regions surrounding the closely-separated LAEs in our sample. Future spectroscopic follow-up of these LAEs, as well as spectroscopy and deep photometry focusing on fainter galaxies in the surrounding area are necessary to place further constraints on the size of the ionized bubbles in those regions. Further, we note that our LAE pair at  $z = 6.046$  is UV-bright ( $M_{UV} \sim -21$ ), similar to that of the closely separated LAEs discussed in Endsley *et al.* (2021a), potentially indicating that UV-bright galaxies in overdense regions enhance Ly $\alpha$  transmission (Endsley *et al.*, 2021a; Endsley & Stark, 2022). Reionization simulation has also predicted that reionization is more advanced in high-density regions compared to those that are isolated, indicating that LAE clustering could lead to Ly $\alpha$  emission that is less-attenuated by the IGM (Qin *et al.*, 2022; Lu *et al.*, 2024). Considering different models for the internal velocity structure of a galaxy (i.e. expanding shell or cloud), Yajima *et al.* (2018) find that the overlapping bubbles are likely to affect the outflow velocity. Further, LAE clustering during reionization supports an accelerated reionization scenario, suggesting that reionization proceeds faster in regions around such galaxies (see, Endsley *et al.*, 2021a).

## 5. Summary and conclusions

We present spectroscopic properties of 22 newly discovered LAEs at the edge of reionization era ( $5.5 \lesssim z \lesssim 6.6$ ), identified in the MAGPI data. For 17 of them covered in the HSC-Subaru Wide layer, we provide photometric magnitudes and  $2\sigma$  limits (for non-detections) of  $i$ ,  $z$ ,  $y$  broad-band filters. The HSC- $y$  band magnitudes indicate that our LAEs are UV-bright, with rest-frame absolute UV magnitudes  $-19.74 \leq M_{UV} \leq -23.27$ . We summarize our main findings as follows:

i) We observe that for  $z < 6$ , the FWHM distribution of LAEs remains almost uniform with no significant change as luminosity increases. However, for  $z > 6$ , there is a noticeable increase in line width with increasing luminosity. This broadening at high redshifts suggests that high-luminosity LAEs at  $z > 6$  may be located in more highly ionized regions of the IGM, despite the fact that a more neutral IGM would typically narrow the line by scattering more Ly $\alpha$  photons.

ii) We also find that some low-equivalent width ( $EW_0 < 20 \text{ \AA}$ ) LAEs exhibit higher ionizing photon production efficiency. This suggests a possible anti-correlation between the Ly $\alpha$  escape fraction and  $\xi_{ion}$ , as observed in other studies. This anti-correlation might indicate a time delay between the production and escape of ionizing photons in these galaxies, potentially related to supernova activity.

iii) Using the Ly $\alpha$  spectroscopic properties and based on some assumptions, we find that LAEs in our sample can ionize

bubbles of size  $R_B = 0.31 - 0.86 \text{ pMpc}$ . The study also finds a significant linear correlation between bubble radii and Ly $\alpha$  line widths. The correlation is particularly strong in LAEs at  $z > 6$ , supporting the idea that the broadening of Ly $\alpha$  lines at these high redshifts is due to large ionized bubbles around those galaxies. Larger bubbles allow most of the Ly $\alpha$  photons to escape the galaxy with minimal scattering in the IGM. Based on simple model and assumptions, Ly $\alpha$  line width can be used to constrain the IGM transmission as well as bubble sizes. A narrow line width could indicate low H I column density, which will force Ly $\alpha$  photons to escape close to the line centre, where line flux is significantly reduced due to IGM scattering. However, this can be uncertain and depends on the complex radiative transfer of Ly $\alpha$  photons in the IGM and CGM. We also discuss that the enhanced visibility of Ly $\alpha$  could also be due to several other factors such as large velocity offset of Ly $\alpha$  form systemic velocity, hardness of ionizing field and due to large peculiar motions of gas clumps present in the galaxy. In such cases, wide Ly $\alpha$  can transmit through the neutral IGM even when the ionized bubble size is small.

iv) Two closely-separated LAE pairs are discovered in two MAGPI fields. One pair at  $z = 6.046$  is just  $3''$  apart on the sky, which corresponds to a physical separation of about 15.92 kpc. Their bubble radii indicate that they sit inside a single large ionized region. As far as we know, this is the pair of LAEs with the smallest separation ever identified in the reionization era. Such overlap of ionized bubbles due to clustering of LAEs during reionization increases the size of the ionized regions and enhances the transmission of Ly $\alpha$  through the neutral IGM. Future spectroscopic and photometric follow-up of the area surrounding these LAEs will detect fainter galaxies, allowing for improved constraints on the size of the ionized bubbles in those regions.

This study shows how wide-area Ly $\alpha$  spectroscopy across a broad range of redshifts can aid in identifying and characterizing ionized bubbles formed during reionization. In the future, as new reionization-era LAEs will be discovered in the upcoming MAGPI fields, it will be possible to place more precise constraints on the evolution of line width with luminosity. Additionally, spectroscopic follow-up using infrared spectroscopy will allow for the measurement of systemic redshifts, leading to more accurate determinations of bubble sizes.

## Acknowledgement

We thank the anonymous referee for their constructive feedback that helped to improve this work. We wish to thank the ESO staff, and in particular the staff at Paranal Observatory, for carrying out the MAGPI observations. MAGPI targets were selected from GAMA. GAMA is a joint European-Australasian project based around a spectroscopic campaign using the Anglo-Australian Telescope. GAMA was funded by the STFC (UK), the ARC (Australia), the AAO, and the participating institutions. GAMA photometry is based on observations made with ESO Telescopes at the La Silla Paranal Observatory under programme ID 179.A-2004, ID 177.A-3016. The MAGPI team acknowledge support from the Aus-

tralian Research Council Centre of Excellence for All Sky Astrophysics in 3 Dimensions (ASTRO 3D), through project number CE170100013.

The Hyper Suprime-Cam (HSC) collaboration includes the astronomical communities of Japan and Taiwan, and Princeton University. The HSC instrumentation and software were developed by the National Astronomical Observatory of Japan (NAOJ), the Kavli Institute for the Physics and Mathematics of the Universe (Kavli IPMU), the University of Tokyo, the High Energy Accelerator Research Organization (KEK), the Academia Sinica Institute for Astronomy and Astrophysics in Taiwan (ASIAA), and Princeton University. Funding was contributed by the FIRST program from Japanese Cabinet Office, the Ministry of Education, Culture, Sports, Science and Technology (MEXT), the Japan Society for the Promotion of Science (JSPS), Japan Science and Technology Agency (JST), the Toray Science Foundation, NAOJ, Kavli IPMU, KEK, ASIAA, and Princeton University.

This paper is based on data collected at the Subaru Telescope and retrieved from the HSC data archive system, which is operated by the Subaru Telescope and Astronomy Data Center (ADC) at NAOJ. Data analysis was in part carried out with the cooperation of Center for Computational Astrophysics (CfCA), NAOJ.

SGL acknowledge the financial support from the MICIU with funding from the European Union NextGenerationEU and Generalitat Valenciana in the call Programa de Planes Complementarios de I+D+i (PRTR 2022) Project (VAL-JPAS), reference ASFAE/2022/025. KEH acknowledges funding from the Australian Research Council (ARC) Discovery Project DP210101945. SMS acknowledges funding from the Australian Research Council (DE220100003). Parts of this research were conducted by the Australian Research Council Centre of Excellence for All Sky Astrophysics in 3 Dimensions (ASTRO 3D), through project number CE170100013. LMV acknowledges support by the German Academic Scholarship Foundation (Studienstiftung des deutschen Volkes) and the Marianne-Plehn-Program of the Elite Network of Bavaria.

## References

- Aihara, H., Arimoto, N., Armstrong, R., et al. 2018, *PASJ*, 70, S4  
Aihara, H., AlSayyad, Y., Ando, M., et al. 2019, *PASJ*, 71, 114  
Bacon, R., Accardo, M., Adjali, L., et al. 2010, in *Society of Photo-Optical Instrumentation Engineers (SPIE) Conference Series*, Vol. 7735, *Ground-based and Airborne Instrumentation for Astronomy III*, ed. I. S. McLean, S. K. Ramsay, & H. Takami, 773508  
Bacon, R., Brinchmann, J., Conseil, S., et al. 2023, *A&A*, 670, A4  
Bagley, M. B., Scarlata, C., Henry, A., et al. 2017, *ApJ*, 837, 11  
Becker, G. D., Bolton, J. S., Madau, P., et al. 2015, *MNRAS*, 447, 3402  
Begley, R., Cullen, F., McLure, R. J., et al. 2024, *MNRAS*, 527, 4040  
Bosman, S. E. I., Davies, F. B., Becker, G. D., et al. 2022, *MNRAS*, 514, 55  
Bouwens, R. J., Smit, R., Labbé, I., et al. 2016, *ApJ*, 831, 176  
Bouwens, R. J., Illingworth, G. D., Oesch, P. A., et al. 2014, *ApJ*, 793, 115  
Bruzual, G., & Charlot, S. 2003, *MNRAS*, 344, 1000  
Cain, C., D'Aloisio, A., Gangolli, N., & Becker, G. D. 2021, *ApJ*, 917, L37  
Castellano, M., Dayal, P., Pentericci, L., et al. 2016, *ApJ*, 818, L3  
Castellano, M., Pentericci, L., Vanzella, E., et al. 2018, *ApJ*, 863, L3  
Cen, R., & Haiman, Z. 2000, *ApJ*, 542, L75  
Chen, Z., Stark, D. P., Mason, C., et al. 2024, *MNRAS*, 528, 7052  
Chisholm, J., Gazagnes, S., Schaerer, D., et al. 2018, *A&A*, 616, A30  
Choustikov, N., Katz, H., Saxena, A., et al. 2024, *MNRAS*, 529, 3751  
Claeysens, A., Richard, J., Blaizot, J., et al. 2019, *MNRAS*, 489, 5022  
Dayal, P., Volonteri, M., Choudhury, T. R., et al. 2020, *MNRAS*, 495, 3065  
Dijkstra, M. 2017, arXiv e-prints, arXiv:1704.03416  
Dijkstra, M., Mesinger, A., & Wyithe, J. S. B. 2011, *MNRAS*, 414, 2139  
Driver, S. P., Hill, D. T., Kelvin, L. S., et al. 2011, *MNRAS*, 413, 971  
Dunlop, J. S., Rogers, A. B., McLure, R. J., et al. 2013, *MNRAS*, 432, 3520  
Endsley, R., & Stark, D. P. 2022, *MNRAS*, 511, 6042  
Endsley, R., Stark, D. P., Charlot, S., et al. 2021a, *MNRAS*, 502, 6044  
Endsley, R., Stark, D. P., Chevallard, J., & Charlot, S. 2021b, *MNRAS*, 500, 5229  
Endsley, R., Stark, D. P., Bouwens, R. J., et al. 2022, *MNRAS*, 517, 5642  
Fan, X., Strauss, M. A., Becker, R. H., et al. 2006, *AJ*, 132, 117  
Finkelstein, S. L., D'Aloisio, A., Paardekooper, J.-P., et al. 2019, *ApJ*, 879, 36  
Flury, S. R., Jaskot, A. E., Ferguson, H. C., et al. 2022, *ApJ*, 930, 126  
Foster, C., Mendel, J. T., Lagos, C. D. P., et al. 2021, *PASA*, 38, e031  
Furtak, L. J., Plat, A., Zitrin, A., et al. 2022, *MNRAS*, 516, 1373  
Gazagnes, S., Chisholm, J., Schaerer, D., Verhamme, A., & Izotov, Y. 2020, *A&A*, 639, A85  
Graham, A. W., & Driver, S. P. 2005, *PASA*, 22, 118  
Guaita, L., Melinder, J., Hayes, M., et al. 2015, *A&A*, 576, A51  
Gupta, A., Trott, C. M., Jaiswar, R., et al. 2024, *ApJ*, 973, 169  
Harikane, Y., Ouchi, M., Shibuya, T., et al. 2018, *ApJ*, 859, 84  
Hashimoto, T., Garel, T., Guiderdoni, B., et al. 2017, *A&A*, 608, A10  
Hayes, M. J., Runnholm, A., Gronke, M., & Scarlata, C. 2021, *ApJ*, 908, 36  
Hayes, M. J., & Scarlata, C. 2023, *ApJ*, 954, L14  
Henry, A., Scarlata, C., Martin, C. L., & Erb, D. 2015, *ApJ*, 809, 19  
Herenz, E. C., & Wisotzki, L. 2017, *A&A*, 602, A111  
Herenz, E. C., Urrutia, T., Wisotzki, L., et al. 2017, *A&A*, 606, A12  
Hinton, S. R., Davis, T. M., Lidman, M., Glazebrook, K., & Lewis, G. F. 2016, *Astronomy and Computing*, 15, 61  
Hoag, A., Bradač, M., Huang, K., et al. 2019, *ApJ*, 878, 12  
Hu, E. M., Cowie, L. L., Barger, A. J., et al. 2010, *ApJ*, 725, 394  
Hu, E. M., Cowie, L. L., Songaila, A., et al. 2016, *ApJ*, 825, L7  
Hu, W., Wang, J., Zheng, Z.-Y., et al. 2017, *ApJ*, 845, L16  
Inoue, A. K., Shimizu, I., Iwata, I., & Tanaka, M. 2014, *MNRAS*, 442, 1805  
Izotov, Y. I., Schaerer, D., Worseck, G., et al. 2020, *MNRAS*, 491, 468  
Izotov, Y. I., Worseck, G., Schaerer, D., et al. 2018, *MNRAS*, 478, 4851  
Jones, G. C., Bunker, A. J., Saxena, A., et al. 2024, arXiv e-prints, arXiv:2409.06405  
Jung, I., Papovich, C., Finkelstein, S. L., et al. 2022a, *ApJ*, 933, 87  
Jung, I., Finkelstein, S. L., Larson, R. L., et al. 2022b, arXiv e-prints, arXiv:2212.09850  
Jung, I., Finkelstein, S. L., Arrabal Haro, P., et al. 2024, *ApJ*, 967, 73  
Kakiichi, K., Dijkstra, M., Ciardi, B., & Graziani, L. 2016, *MNRAS*, 463, 4019  
Kakiichi, K., & Gronke, M. 2021, *ApJ*, 908, 30  
Katz, H., Āurovčiková, D., Kimm, T., et al. 2020, *MNRAS*, 498, 164  
Katz, H., Garel, T., Rosdahl, J., et al. 2022, *MNRAS*, 515, 4265  
Kennicutt, Robert C., J. 1998, *ARA&A*, 36, 189  
Kerutt, J., Wisotzki, L., Verhamme, A., et al. 2022, *A&A*, 659, A183  
Kerutt, J., Oesch, P. A., Wisotzki, L., et al. 2024, *A&A*, 684, A42  
Konno, A., Ouchi, M., Ono, Y., et al. 2014, *ApJ*, 797, 16  
Konno, A., Ouchi, M., Shibuya, T., et al. 2018, *PASJ*, 70, S16  
Kulkarni, G., Keating, L. C., Haehnelt, M. G., et al. 2019, *MNRAS*, 485, L24  
Laursen, P., Sommer-Larsen, J., Milvang-Jensen, B., Fynbo, J. P. U., & Razoumov, A. O. 2019, *A&A*, 627, A84  
Li, Z., & Gronke, M. 2022, *MNRAS*, 513, 5034  
Lin, X., Cai, Z., Wu, Y., et al. 2024, *ApJS*, 272, 33

Lu, T.-Y., Mason, C. A., Hutter, A., et al. 2024, *MNRAS*, 528, 4872

Mainali, R., Zitrin, A., Stark, D. P., et al. 2018, *MNRAS*, 479, 1180

Maji, M., Verhamme, A., Rosdahl, J., et al. 2022, *A&A*, 663, A66

Malhotra, S., & Rhoads, J. E. 2006, *ApJ*, 647, L95

Mascia, S., Pentericci, L., Calabrò, A., et al. 2023, *A&A*, 672, A155

Maseda, M. V., Bacon, R., Lam, D., et al. 2020, *MNRAS*, 493, 5120

Mason, C. A., & Gronke, M. 2020, *MNRAS*, 499, 1395

Mason, C. A., Treu, T., de Barros, S., et al. 2018, *ApJ*, 857, L11

Matthee, J., Sobral, D., Best, P., et al. 2017a, *MNRAS*, 465, 3637

Matthee, J., Sobral, D., Darvish, B., et al. 2017b, *MNRAS*, 472, 772

Matthee, J., Sobral, D., Santos, S., et al. 2015, *MNRAS*, 451, 400

Matthee, J., Naidu, R. P., Pezzulli, G., et al. 2022, *MNRAS*, 512, 5960

Meyer, R. A., Laporte, N., Ellis, R. S., Verhamme, A., & Garel, T. 2021, *MNRAS*, 500, 558

Miyazaki, S., Komiyama, Y., Kawanomoto, S., et al. 2018, *PASJ*, 70, S1

Mukherjee, T., Zafar, T., Nanayakkara, T., et al. 2023, *A&A*, 680, L5

Naidu, R. P., Tacchella, S., Mason, C. A., et al. 2020, *ApJ*, 892, 109

Naidu, R. P., Matthee, J., Oesch, P. A., et al. 2022, *MNRAS*, 510, 4582

Nakajima, K., Ellis, R. S., Robertson, B. E., Tang, M., & Stark, D. P. 2020, *ApJ*, 889, 161

Nakane, M., Ouchi, M., Nakajima, K., et al. 2024, *ApJ*, 967, 28

Napolitano, L., Pentericci, L., Santini, P., et al. 2024, *A&A*, 688, A106

Neufeld, D. A. 1990, *ApJ*, 350, 216

Ning, Y., Cai, Z., Jiang, L., et al. 2023, *ApJ*, 944, L1

Pentericci, L., Fontana, A., Vanzella, E., et al. 2011, *ApJ*, 743, 132

Pentericci, L., Vanzella, E., Fontana, A., et al. 2014, *ApJ*, 793, 113

Prieto-Lyon, G., Strait, V., Mason, C. A., et al. 2023, *A&A*, 672, A186

Pucha, R., Reddy, N. A., Dey, A., et al. 2022, *AJ*, 164, 159

Qin, Y., Wyithe, J. S. B., Oesch, P. A., et al. 2022, *MNRAS*, 510, 3858

Robertson, B. E., Ellis, R. S., Dunlop, J. S., McLure, R. J., & Stark, D. P. 2010, *Nature*, 468, 49

Robertson, B. E., Ellis, R. S., Furlanetto, S. R., & Dunlop, J. S. 2015, *ApJ*, 802, L19

Roy, N., Henry, A., Treu, T., et al. 2023, *ApJ*, 952, L14

Santos, S., Sobral, D., & Matthee, J. 2016, *MNRAS*, 463, 1678

Saxena, A., Bunker, A. J., Jones, G. C., et al. 2024, *A&A*, 684, A84

Schaerer, D. 2003, *A&A*, 397, 527

Schaerer, D., Izotov, Y. I., Wörseck, G., et al. 2022, *A&A*, 658, L11

Shibuya, T., Ouchi, M., Nakajima, K., et al. 2014, *ApJ*, 788, 74

Shibuya, T., Ouchi, M., Harikane, Y., et al. 2018, *PASJ*, 70, S15

Shivaei, I., Reddy, N. A., Siana, B., et al. 2018, *ApJ*, 855, 42

Simmonds, C., Tacchella, S., Maseda, M., et al. 2023, *MNRAS*, 523, 5468

Smith, A., Kannan, R., Garaldi, E., et al. 2022, *MNRAS*, 512, 3243

Sobral, D., & Matthee, J. 2019, *A&A*, 623, A157

Songaila, A., Barger, A. J., Cowie, L. L., Hu, E. M., & Taylor, A. J. 2022, *ApJ*, 935, 52

Songaila, A., Cowie, L. L., Barger, A. J., Hu, E. M., & Taylor, A. J. 2024, *arXiv e-prints*, arXiv:2407.08772

Songaila, A., Hu, E. M., Barger, A. J., et al. 2018, *ApJ*, 859, 91

Stark, D. P., Ellis, R. S., Charlot, S., et al. 2017, *MNRAS*, 464, 469

Steidel, C. C., Bogosavljević, M., Shapley, A. E., et al. 2018, *ApJ*, 869, 123

Tacchella, S., Bose, S., Conroy, C., Eisenstein, D. J., & Johnson, B. D. 2018, *ApJ*, 868, 92

Tang, M., Stark, D. P., Topping, M. W., Mason, C., & Ellis, R. S. 2024a, *arXiv e-prints*, arXiv:2408.01507

Tang, M., Stark, D. P., Chen, Z., et al. 2023, *MNRAS*, 526, 1657

Tang, M., Stark, D. P., Ellis, R. S., et al. 2024b, *MNRAS*, 531, 2701

Taylor, A. J., Barger, A. J., Cowie, L. L., Hu, E. M., & Songaila, A. 2020, *ApJ*, 895, 132

Taylor, A. J., Cowie, L. L., Barger, A. J., Hu, E. M., & Songaila, A. 2021, *ApJ*, 914, 79

Tilvi, V., Papovich, C., Finkelstein, S. L., et al. 2014, *ApJ*, 794, 5

Tilvi, V., Malhotra, S., Rhoads, J. E., et al. 2020, *ApJ*, 891, L10

Torralba-Torregrosa, A., Matthee, J., Naidu, R. P., et al. 2024, *arXiv e-prints*, arXiv:2404.10040

Umeda, H., Ouchi, M., Nakajima, K., et al. 2023, *arXiv e-prints*, arXiv:2306.00487

Urrutia, T., Wisotzki, L., Kerutt, J., et al. 2019, *A&A*, 624, A141

Valentino, F., Brammer, G., Fujimoto, S., et al. 2022, *ApJ*, 929, L9

Verhamme, A., Orlitová, I., Schaerer, D., & Hayes, M. 2015, *A&A*, 578, A7

Verhamme, A., Orlitová, I., Schaerer, D., et al. 2017, *A&A*, 597, A13

Verhamme, A., Garel, T., Ventou, E., et al. 2018, *MNRAS*, 478, L60

Weilbacher, P. M., Palsa, R., Streicher, O., et al. 2020, *A&A*, 641, A28

Weinberger, L. H., Kulkarni, G., Haehnelt, M. G., Choudhury, T. R., & Puchwein, E. 2018, *MNRAS*, 479, 2564

Whitler, L., Endsley, R., Stark, D. P., et al. 2023, *MNRAS*, 519, 157

Whitler, L., Stark, D. P., Endsley, R., et al. 2024, *MNRAS*, 529, 855

Whitler, L. R., Mason, C. A., Ren, K., et al. 2020, *MNRAS*, 495, 3602

Witstok, J., Smit, R., Saxena, A., et al. 2024, *A&A*, 682, A40

Witten, C., Laporte, N., Martin-Alvarez, S., et al. 2024, *Nature Astronomy*, 8, 384

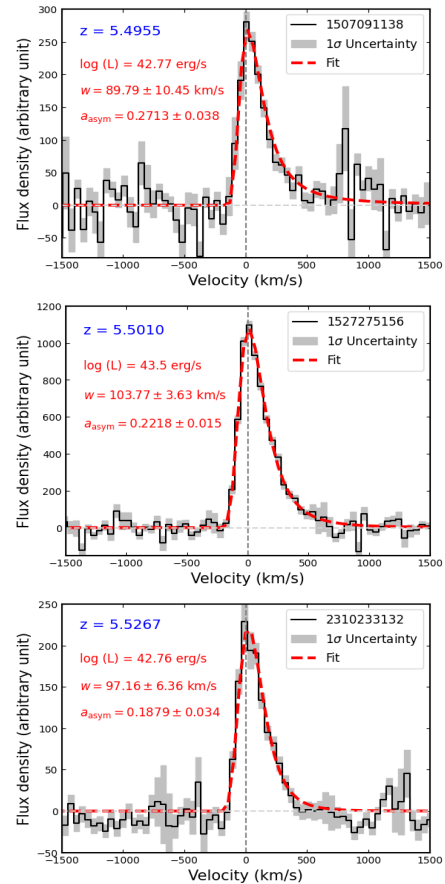
Witten, C. E. C., Laporte, N., & Katz, H. 2023, *ApJ*, 944, 61

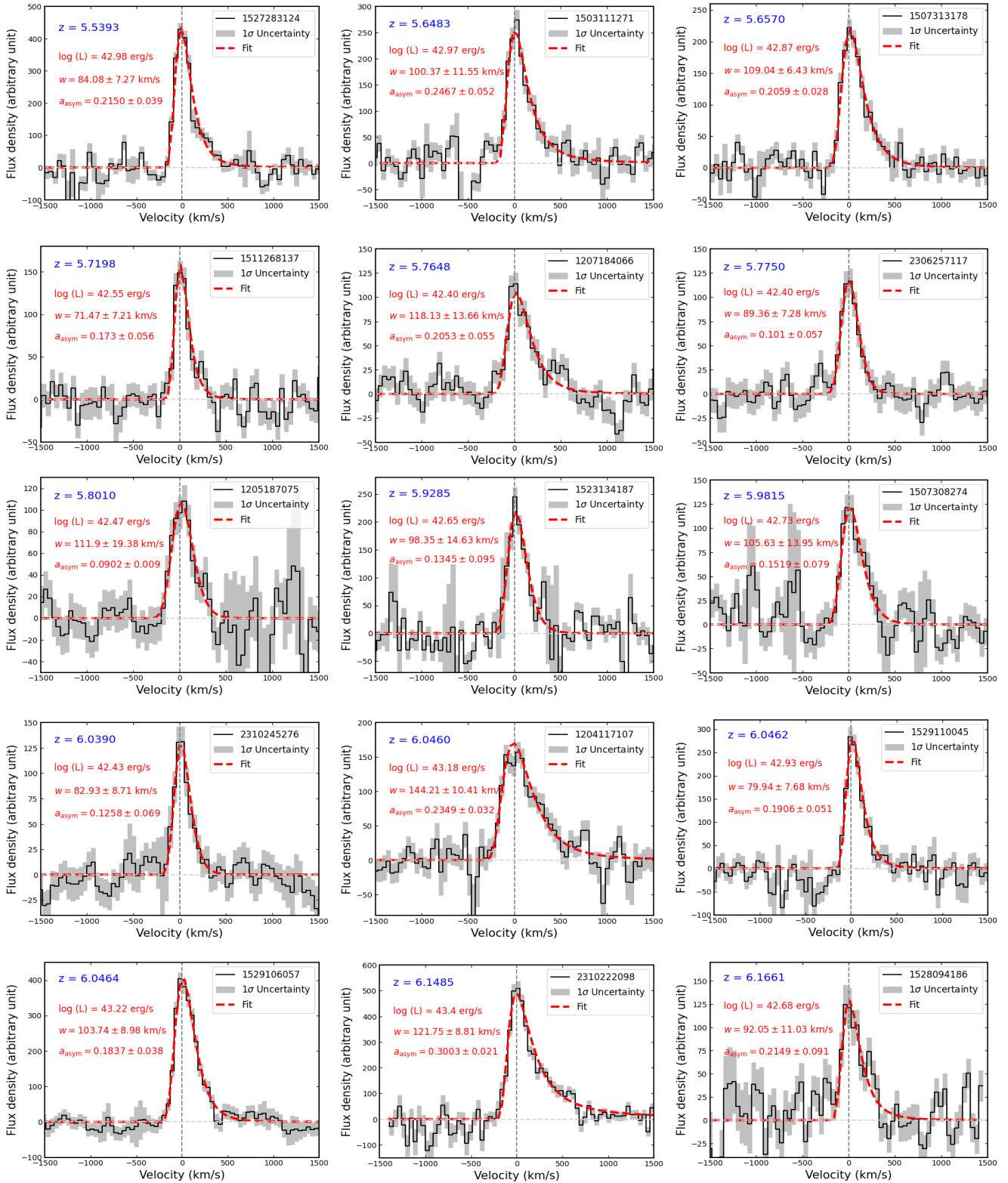
Xu, X., Henry, A., Heckman, T., et al. 2022, *ApJ*, 933, 202

Yajima, H., Sugimura, K., & Hasegawa, K. 2018, *MNRAS*, 477, 5406

Yang, H., Malhotra, S., Gronke, M., et al. 2017, *ApJ*, 844, 171

## Appendix 1. Fitting Ly $\alpha$ lines





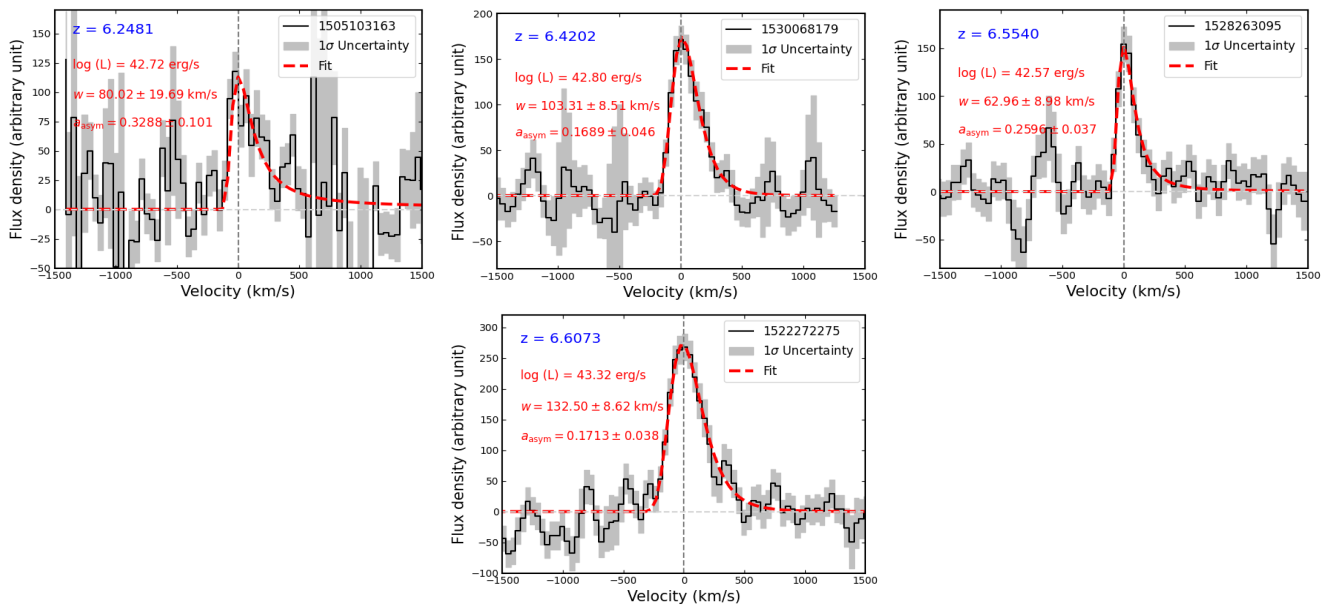


**Figure 6.** Shown are the velocity profiles of 22 LAEs at  $5.5 \lesssim z \lesssim 6.6$ . 1D spectrum (solid black, named by corresponding MAGPI ID) and associated  $\pm 1\sigma$  uncertainty on the flux density (grey shaded), along with the asymmetric Gaussian fit (dashed-red) to the spectrum for each LAE are presented in each panels. In each panel, luminosity, redshift and best-fit parameters such as  $w$  defining FWHM, and asymmetry parameter are given in the left corners.